Journal of Alloys and Compounds 508 (2010) 85–93

Contents lists available at ScienceDirect

Journal of Alloys and Compounds

journal homepage: www.elsevier.com/locate/jallcom

Thermal cycling behavior of $La_2Zr_2O_7$ coating with the addition of Y_2O_3 by EB-PVD

Zhenhua Xu[a,b,c], Limin He[c,*], Xiaolong Chen[a], Yu Zhao[a], Rende Mu[c], Shimei He[c], Xueqiang Cao[a,**]

[a] State Key Laboratory of Rare Earth Resources Utilization, Changchun Institute of Applied Chemistry, Chinese Academy of Sciences, Changchun 130022, China
[b] Graduate School of Chinese Academy of Sciences, Beijing 100039, China
[c] Beijing Institute of Aeronautical Materials, Department 5, P.O. Box 81-5, Beijing 100095, China

ARTICLE INFO

Article history:
Received 31 March 2010
Received in revised form 10 April 2010
Accepted 15 April 2010
Available online 22 April 2010

Keywords:
Thermal barrier coatings
EB-PVD
$La_2Zr_2O_7$
Y_2O_3
Thermal cycling

ABSTRACT

Thermal barrier coatings (TBCs) of $La_2Zr_2O_7$ (LZ) with the addition of 3 wt.% Y_2O_3 (LZ3Y) were deposited by electron beam-physical vapor deposition (EB-PVD). The phase structures, surface and cross-sectional morphologies, cyclic oxidation behaviors of these coatings were studied in detail. The thermal cycling test at 1373 K in an air furnace indicates that the LZ3Y coating has a lifetime of 617 cycles which is about 10% longer than that of LZ coating. The improvement of chemical homogeneity of the coating, the superior growth behavior of columns and the favorable mechanical properties are all very helpful to the prolongation of thermal cycling life of LZ3Y coating. The failure of LZ and LZ3Y coatings is mainly a result of the excess La_2O_3, the chemical incompatibility of ceramic coatings with TGO layer, the thermal expansion mismatch between ceramic coatings and bond coat, and the outward diffusion of alloying elements into the ceramic coatings.

1. Introduction

TBCs prepared by EB-PVD are widely used to protect the hot-section parts of aircraft engine turbines and to meet the rapidly increasing demands for higher fuel efficiency and greater thrust due to the high strain compliance of the segmented columnar structure of EB-PVD coatings [1]. Up to now, the most successful TBC material is 6–8 wt.% yttria stabilized zirconia (YSZ), which are applied on engine hot-section components by plasma spraying (PS) or EB-PVD [2]. However, a major disadvantage of YSZ is the limited operation temperature of 1473 K for long-term application. Above 1473 K, phase transformations from the t'-tetragonal to tetragonal and cubic ($t+c$) and then to monoclinic (m) occur, leading to the failure of TBCs [3]. Moreover, the sintering-induced volume shrinkages would degrade the columnar structure of EB-PVD coating and increase the elasticity modulus and, as a result, reduce the favorable strain tolerance of the coating [4]. In the next generation of advanced engines, further increase in thrust-to-weight ratio will require even higher gas inlet temperature. Hence it has motivated a search for alternate TBCs with even lower thermal conductivity, higher operation temperature, better sintering resistance and phase stability at even higher temperature for future improvements in engine's performance.

Among the numerous oxides that have been explored as alternate TBCs materials, the rare earth zirconates have been investigated and the results indicate that these materials are significant for the top ceramic materials for future TBCs. Especially those materials with pyrochlore-based structures and high melting points show promising thermo-physical properties. Lanthanum zirconate ($La_2Zr_2O_7$, LZ) has a lower thermal conductivity ($1.56\,W\,m^{-1}\,K^{-1}$, 1273 K) than YSZ, a cubic pyrochlore structure which is stable up to its melting point (2573 K), and it has been proposed as a promising TBCs material [4–10]. The LZ crystal structure consists of the corner-shared ZrO_6 octahedra forming the backbone of the network and La^{3+} ions fill the holes which are formed by six ZrO_6 octahedra. It can largely tolerate vacancies at the La^{3+}, Zr^{4+}, and O^{2-} sites without phase transformation. Both La^{3+} and Zr^{4+} sites can be substituted by a lot of other elements with similar ionic radii in cases the electrical neutrality is satisfied, giving rise to the possibility of tailoring its thermal properties [6,11]. It was demonstrated that LZ coating had been fabricated by EB-PVD [4,10,12,13], La and Zr are not equally distributed in the coating during deposition due to evaporation differences of La_2O_3 and ZrO_2. Literature data on vapor pressures predict a difference of three orders of magnitude between La_2O_3 and ZrO_2 at 3273 K [4]. If vapor pressures of oxide components fall too far apart from each other as suspected in the present case, selective evaporation and selective deposition may occur. In order to overcome this problem, presence of a lower vapor

---

* Corresponding author. Tel.: +86 10 62496456; fax: +86 10 62496456.
** Corresponding author. Tel.: +86 431 85262285; fax: +86 431 85262285.
E-mail addresses: he_limin@yahoo.com (L. He), xcao@ciac.jl.cn (X. Cao).

0925-8388/$ – see front matter © 2010 Elsevier B.V. All rights reserved.
doi:10.1016/j.jallcom.2010.04.124

pressure oxide such as Y_2O_3 helps to moderate the excessive vapor pressure condition during deposition as well as the growth conditions in favor of pertinent pyrochlore structure formation [4,14]. Saruhan et al. [4,14] confirmed that 3 wt.% Y_2O_3 addition in LZ (LZ3Y) could improve the chemical homogeneity of its coating. In addition, LZ ceramics doped with various Y_2O_3 contents have been investigated in previous paper and the optimized content of 3 wt.% Y_2O_3 as candidate for TBCs is also confirmed [15].

However, LZ3Y coating has not been investigated in detail up to now, and no thermal cycling life result is available. In the present work, the phase structures, columnar microstructures, surface and cross-sectional morphologies and thermal cycling behaviors of both LZ and LZ3Y coatings prepared by EB-PVD are studied in detail.

2. Experimental

2.1. Ingots of LZ and LZ3Y coatings

LZ and LZ3Y powders were synthesized by solid-state reaction at 1673 K for 12 h with La_2O_3, ZrO_2 and Y_2O_3 as the starting materials. The deionized water-based suspensions of LZ and LZ3Y powders were ball-milled for 24 h with zirconia balls, respectively. After the cast-formation, the ingots were densified at 1773 K for 12 h.

2.2. Preparation of bond coat and top ceramic coatings

The directionally solidified Ni-based superalloy DZ125 (30 mm × 10 mm × 1.5 mm) was used as the substrate material. The substrates were ground before the bond coats (BC) of NiCrAlYSi were deposited by arc ion plating (A-1000 Vacuum Arc Ion-Plating Unit). The BC used identically in this study had a nominal composition (wt.%): 20–25Cr, 6–10Al, 0.08–0.4Y, 0.4–0.8Si, and Ni as balance. After the deposition of BC, the substrates were heat-treated under high vacuum at 1143 K for 3 h. The purpose of heat treatment at 1143 K before EB-PVD deposition was to enhance the adhesion of bond coat to substrate due to interdiffusion between them. The top ceramic coatings of LZ3Y and LZ were fabricated by EB-PVD. The current of electron beam was in the range of 500–700 mA. Meanwhile, the accelerated high voltage (kV) was in the range of −9.52 to −10.23. The deposition pressure of EB-PVD working chamber was about 1×10^{-2} Pa and no oxygen was introduced into the vacuum chamber. The average substrate temperature was ∼1173 K and the rotation speed was 7 rpm.

2.3. Cyclic oxidation tests

To evaluate the thermal shock resistance of the coatings, cyclic oxidation tests were carried out by heating in an air furnace at 1373 K for 30 min followed by removing out for cooling-down with airflow for 5 min. The heating-up and then cooling-down makes one oxidation cycle, and this process was repeated until 5% area of the coating was lost, and the cycling number was then regarded as the thermal cycling life of TBCs. Meanwhile, after the cyclic oxidation for a certain time, the samples were also weighted with a balance, and the weight changes as a function of oxidation time were recorded.

2.4. Characterizations

Small bars of sintered specimens of both LZ and LZ3Y were prepared by cold pressing followed by pressureless sintering at 1923 K for 12 h. Such small bars were further used for the measurements of mechanical properties. Before the indentation test, the surfaces of the densified samples were polished with diamond suspensions (Metadi Diamond 15–1 μm, Buehler) by a low-speed automatic polisher (Minimet 1000, Buehler). Vicker's microhardnesses of both LZ and LZ3Y were measured by a microindentor (Struers Duramin Ver. 2.02) with a load of 4.9 N for 15 s. The fracture toughness (K_{IC}) was estimated from the crack length [16]:

$$K_{IC} = 0.16 \cdot H_v \cdot a^{1/2} \cdot (c/a)^{-2/3} \quad (1)$$

where H_v is hardness, $2c$ is the crack and impression length and $2a$ is the length of the indent diagonal. The sample dimension for Young's modulus measurement (Instron Model 1121) was about 24 mm × 4 mm × 1.3 mm.

The coatings were embedded in a transparent cold-setting epoxy and polished with diamond pastes down to 1 μm. Scanning electron microscope (SEM, FEI-Quanta 600) equipped with energy dispersive spectroscopy (EDS, Oxford INCAx-sight 6427) was applied for the microstructure and composition evaluation. XRD (Bruker D8 Advance) with Cu-K_α radiation at a scan rate of 10° min^{-1} was employed to analyze the phase structures of the two ingots and coatings. In order to evaluate the lattice parameter, the silicon powder was used as the external standard. Raman spectrum was recorded at room temperature with T64000 modular triple Raman system (Horiba Jobin Yvon, France). The 514.5 nm line of an argon ion laser (Stabilite 2017, Spectra-Physics Lasers Inc., USA) was used as the excitation line. Laser power of 5 mW was incident on the sample in a 2 μm diameter spot through a standard microscope objective lens. The Raman spectrum was collected with a data point acquisition time of 90 s and a spectral range of 100–1000 cm^{-1}.

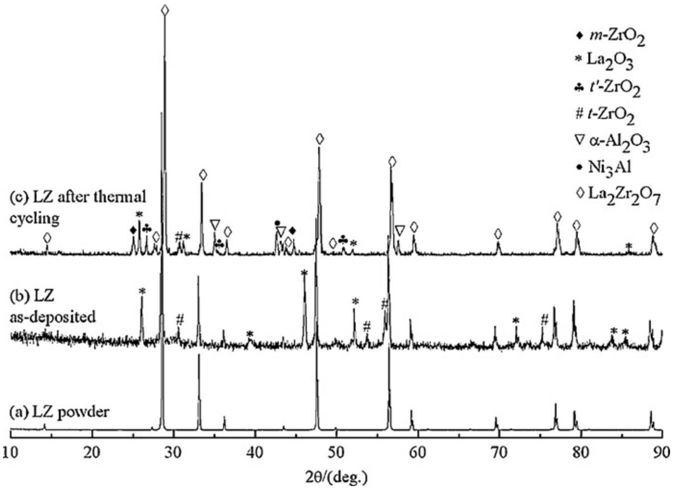

Fig. 1. XRD patterns of LZ: starting powder (a), as-deposited coating (b) and coating after thermal cycling (c).

3. Results and discussion

3.1. Phase structure of the coating

For comparison, XRD patterns of the LZ coating surface before and after thermal cycling are presented in Fig. 1. The existence of excess La_2O_3 is obviously observed in the as-deposited coating (Fig. 1b), meanwhile, several weak peaks of t-ZrO_2 coexist. The excess La_2O_3 in the coating is dangerous to the coating. It would absorb moisture from air with the formation of $La(OH)_3$, leading to the swelling and then spalling of the coating automatically. It was observed in our experiments that some LZ coatings with a high content of La_2O_3 spalled automatically after being stored for a few days. Therefore, the deposition condition of LZ coating should be properly controlled to keep the content of excess La_2O_3 as low as possible. After thermal cycling, a new phase of m-ZrO_2 induced by phase transition is observed as shown in Fig. 1c. Two new phases belonging to α-Al_2O_3 and Ni_3Al are also observed, implying that partial spallation of LZ coating could occur during thermal cycling and the spallation location of LZ coating probably occurs at the interface of LZ and bond coat. Obviously, those peak intensities which belong to the pyrochlore structure observed in Fig. 1c are correspondingly stronger than those of peaks as shown in Fig. 1b, peaks of La_2O_3 and ZrO_2 are weakened and/or disappeared after long-term exposure, implying that the as-decomposed La_2O_3 and ZrO_2 could be incorporated into the coating. As a result, the pyrochlore structure of LZ can be further formed even though the temperature of thermal cycling test adopted in this study is only 1373 K. This result is in good agreement with the previous investigation of Jarligo et al. [17]. By comparing results of Fig. 1 and Table 1, it is also interest-

Table 1
Lattice parameters of LZ and LZ3Y powders and coatings before and after thermal cycling.

Sample	Item	Lattice parameter (nm)
LZ	Starting powder	1.08061
	As-deposited coating	1.08224
	Coating after thermal cycling	1.07695
LZ3Y	Starting powder	1.08155
	As-deposited coating	1.08114
	Coating after thermal cycling	1.07965

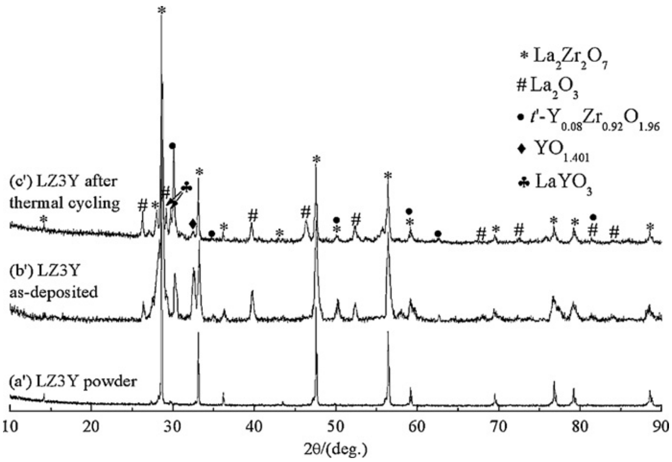

Fig. 2. XRD patterns of LZ3Y: starting powder (a), as-deposited coating (b) and coating after thermal cycling (c).

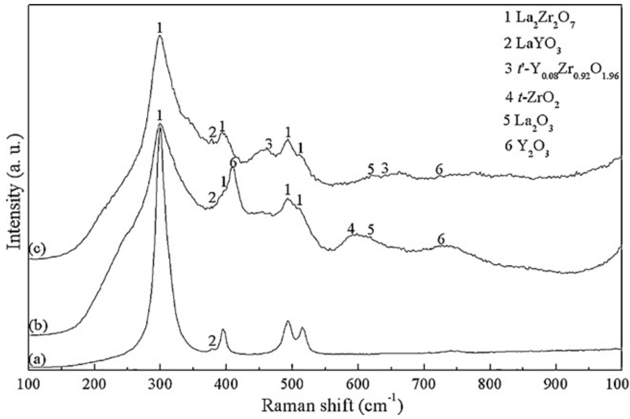

Fig. 3. Raman spectra of LZ3Y: starting powder (a), as-deposited coating (b) and coating after thermal cycling (c).

ing to see that all the peaks (Fig. 1b) slightly shift to the lower 2θ value (the larger d values) in contrast to that of the powder (Fig. 1a). The main reason is that the former has a higher content of La_2O_3 than the latter. La^{3+} (0.116 nm) has a larger ionic radius than Zr^{4+} (0.072 nm). Differently, all the peaks scrutinized in Fig. 1c slightly shift to the larger 2θ value compared with the as-deposited coating, implying that the solubility of ZrO_2 in LZ coating occurs after long-term service. These phenomena are consistent with the variation trend of the lattice parameters for LZ system presented in Table 1.

XRD patterns of LZ3Y coating surface before and after thermal cycling are compared in Fig. 2. For comparison, XRD pattern of the starting powder of LZ3Y is also presented in Fig. 2. Except for several weak peaks (i.e. La_2O_3, t'-$Y_{0.08}Zr_{0.92}O_{1.96}$ and $YO_{1.401}$) as marked in Fig. 2b, the as-deposited LZ3Y coating exhibits XRD pattern similar to its starting powder. The appearance of these unpopular phases is probably attributed to the partial decomposition of LZ3Y ingot during the overheating of EB-PVD. However, intensities of its diffraction peaks are low, indicating that the crystallization is not perfect owing to the fast cooling rate of the electron beam. After thermal cycling, intensities of diffraction peaks are highly intensified because the re-crystallization is basically finished. It can be carefully seen from Fig. 2c that two new peaks of $LaYO_3$ located at 29.19° and 29.69° appear, and the intensity of $YO_{1.401}$ is evidently weakened as compared with the corresponding peak as shown in Fig. 2b. The following may be the reasons for these results:

(1) The chemical reactions:

$$La_2Zr_2O_7 + Y_2O_3 = 2LaYO_3 + 2ZrO_2 \tag{2}$$

$$0.18Y_2O_3 + 1.64ZrO_2 = 2Y_{0.18}Zr_{0.82}O_{1.91} \tag{3}$$

(2) La^{3+} in LZ is partially substituted by Y^{3+}, it will cause the additional chemical reaction which can be expressed as:

$$La_2O_3 + Y_2O_3 = 2LaYO_3 \tag{4}$$

On the other hand, the lattice parameters belonging to pyrochlore structure (LZ) calculated from Fig. 2 are also listed in Table 1. After thermal cycling, the lattice parameter of pyrochlore structure is 1.0797 nm which is approximately 0.0015 nm lower than that of the as-deposited coating. The cyclic oxidation results in a decrement of lattice parameter, implying that the solubility of Y_2O_3 into LZ coating and/or the substitution of La^{3+} in LZ by Y^{3+}. Y^{3+} (0.101 nm) has a lower ionic radius than La^{3+} (0.116 nm), therefore, the substitution of La^{3+} by Y^{3+} would lead to the decrement of lattice parameter of pyrochlore structure. Interestingly, the lattice parameter of pyrochlore structure in the as-deposited LZ3Y coating is mostly identical to the starting powder, demonstrating that LZ3Y coating with pyrochlore structure has been successfully fabricated after optimization of EB-PVD processing conditions.

Laser Raman spectroscopy is a powerful tool to investigate chemical composition in ceramic materials [18]. Fig. 3 shows Raman spectra of LZ3Y starting powder and coatings before and after thermal cycling in the range of 100–1000 cm^{-1} at room temperature. For the three specimens, four Raman bands at 299, 395, 490 and 515 cm^{-1} are visible. These Raman bands are the characteristics of LZ-type structure, which is consistent with the previous results [19]. One Raman band at 375 cm^{-1} is also detected in three specimens, which is the characteristics of $LaYO_3$ according to the Raman spectrum of pure $LaYO_3$. Meanwhile, the peak intensity of $LaYO_3$ is enhanced after thermal cycling, implying that the addition of Y_2O_3 is quite beneficial to the formation of $LaYO_3$ and/or the incorporation into excess La_2O_3 during thermal cycling. Moreover, it is reasonable to explain why Raman peaks belonging to Y_2O_3 are gradually weakened after thermal cycling as compared with the as-deposited coating. Yamaguchi et al. [20] reported that $LaYO_3$ was still stable when the sintering temperature was below 1723 K. Therefore, compared with the LZ coating, the phase stability of LZ3Y coating basically keeps unchanged even the cyclic temperature is only at 1373 K. On the other hand, a new band at 587 cm^{-1} which corresponds to t-ZrO_2 is detected in Fig. 3b, and two Raman bands at 460 and 640 cm^{-1} are assigned to t'-$Y_{0.08}Zr_{0.92}O_{1.96}$ as only shown in Fig. 3c. It demonstrates that the solid solution of Y_2O_3 into ZrO_2 lattice perhaps occurs after long-term exposure. Additionally, one weak band at 619 cm^{-1} which is the characteristic of La_2O_3 is simultaneously detected in Fig. 3b and c. These results are in good agreement with the XRD results shown in Fig. 2.

3.2. Microstructure of the coating

Fig. 4 shows SEM images of the fractured samples of the as-deposited LZ and LZ3Y coatings. It can be seen from Fig. 4 that the feather-like microstructure within the columns normal to the bond coat surface is a representative morphology of the coating made by EB-PVD, and such a columnar structure has a very high tolerance to thermal cycling and is further helpful to the improvement of thermal cycling life [13]. The columns of LZ coating (Fig. 4a) are more regularly distributed and the inter-columnar gaps are narrower compared with the LZ3Y coating (Fig. 4b). The gaps induced by the “shadowing effect” among columns may partially release the thermal stress during long-term service. Namely, the tip edge of a columnar grain blocks the vapor flux and produces a shadow during rotation, which results in formation of inter-columnar gaps [21].

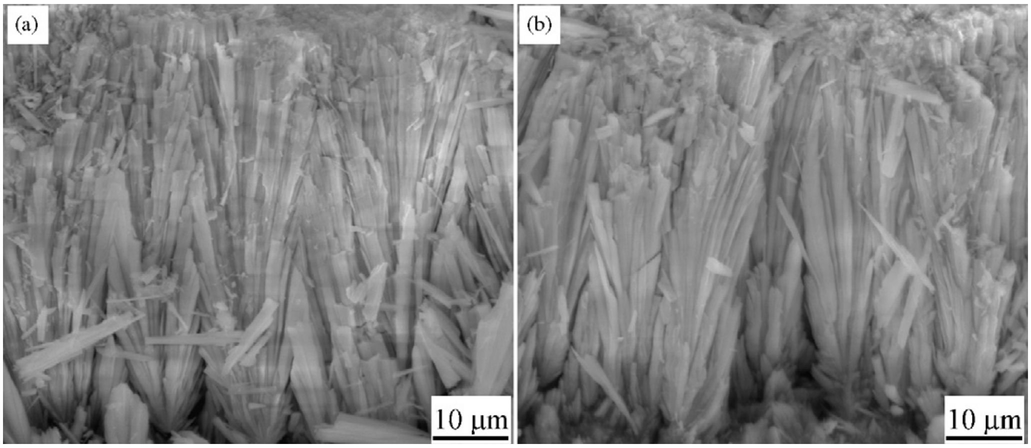

Fig. 4. SEM micrographs of the fractured cross-sections of LZ (a) and LZ3Y (b) coatings.

In addition, the growth of some columns and subcolumns within LZ coating is much denser than that of LZ3Y coating. The bridging of columns within LZ coating could lead to a reduction in strain tolerance and hence may affect TBC life. For the LZ3Y coating, it is clearly found that each column consists of a number of subcolumns with different misorientations. Columns are irregularly distributed and contain some inter-columnar gaps. Moreover, length of each feather-arm is different from each other. The more is the disorder between each column, the lower is the thermal conductivity of the coating [22]. Differences in vapor pressure of the constituents could result in the formation of bubbles in the melting pool and then lead to spitting of liquid droplets from the melting pool onto the substrate. This results in inhomogeneity in the coating microstructure [23]. The columnar morphologies between these two coatings are different, which could be related to the averaged substrate temperature adopted during deposition in combination with the relation of $0.3T_m < T_s < 0.5T_m$ (T_s = substrate temperature and T_m = melting point) [24]. In addition, the morphology of the deposited coatings is generally controlled by multiple processing variables including adatom kinetic energy, adatom angle of incidence, deposition rate, the presence and nature of the surrounding gas, elemental compositions of the adatoms, substrate roughness and the relative amount of chamber ionization generation [25,26].

3.3. *Oxidation and thermal cycling behavior of the coating*

In order to evaluate the performance of LZ3Y coating, the thermal cycling test of LZ coating was also conducted under the same condition. The LZ3Y coating has a lifetime of 617 cycles which corresponds to a total cycling time of 360 h, approximately 10% longer than that of LZ coating (559 cycles). The longer lifetime of LZ3Y coating could be mainly attributed to: (1) the fracture toughness of LZ3Y bulk material is higher than that of LZ bulk material and (2) its Young's modulus (55.17 GPa) is obviously lower than that of LZ (77.37 GPa). In TBCs, residual stress induced by thermal expansion mismatch can be described as [27]:

$$\sigma_R \approx \frac{\Delta a \cdot \Delta T \cdot E_f}{(1-\nu_f)} \tag{5}$$

where σ_R is residual stress, ΔT is the temperature change, $\Delta\alpha$ is thermal expansion coefficient difference between the ceramic coat and substrate, and E_f and ν_f are Young's modulus and Poisson ratio of the coating, respectively. Meanwhile, the strain energy release rate is simply calculated by Eq. (6) [28]:

$$G \approx \frac{\sigma_R^2 \cdot H}{E_f} \tag{6}$$

where G is the strain energy release rate, H is the thickness of the ceramic coating. It can be seen that a lower Young's modulus contributes to a decreased residual stress and store energy for cracking when TBC is cooled down repeatedly during thermal cycling; (3) the content of excess La_2O_3 in the LZ coating is apparently higher than that of LZ3Y coating, which is disadvantageous to improve the resistance to thermal cycling load of the coating and (4) the superior growth behavior of columns is attained in LZ3Y coating.

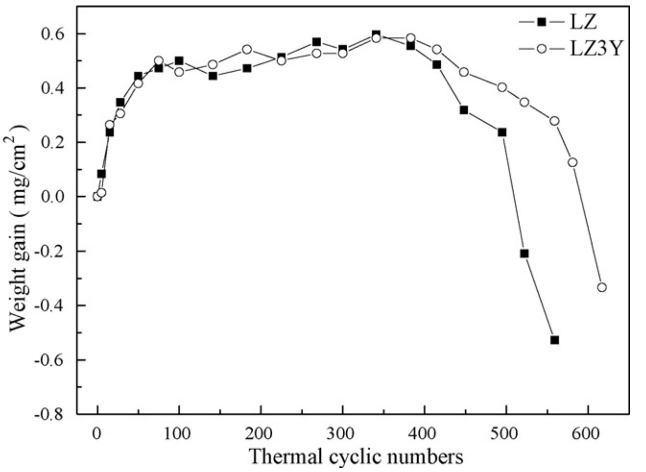

Fig. 5. Weight changes of LZ and LZ3Y coatings as functions of thermal cyclic numbers during cyclic oxidation in air at 1373 K.

The specific weight changes per unit surface area of LZ and LZ3Y coatings as a function of cycling number at 1373 K are shown in Fig. 5. For these two coatings, their weight gains are basically consistent with the parabolic behaviors before 341 cycles, and the parabolic rate constants are correspondingly calculated to be $\sim 8.54 \times 10^{-4}$ and $\sim 8.21 \times 10^{-4}$ $mg^2\,cm^{-4}$ for LZ and LZ3Y coatings, respectively. Their weights are quickly increased in the initial 75 cycles and then decreased after 341 cycles for LZ and 383 cycles for LZ3Y coatings due to the spallation of ceramic coatings. These phenomena observed in Fig. 5 can explain the longer lifetime of LZ3Y than that of LZ coating. The visible weight losses of these two coatings occur after 383 cycles, which could greatly accelerate the coating spallation. In addition, the continuous weight losses of the two coatings after long-term exposure maybe a result of both edges chipping of the ceramic coating and formation of non-adherent spinel phase at those parts of the sides of the specimen, where bond coat surface is free of ceramic coating due to the limit of TBCs processing. On the other hand, the corresponding fitted

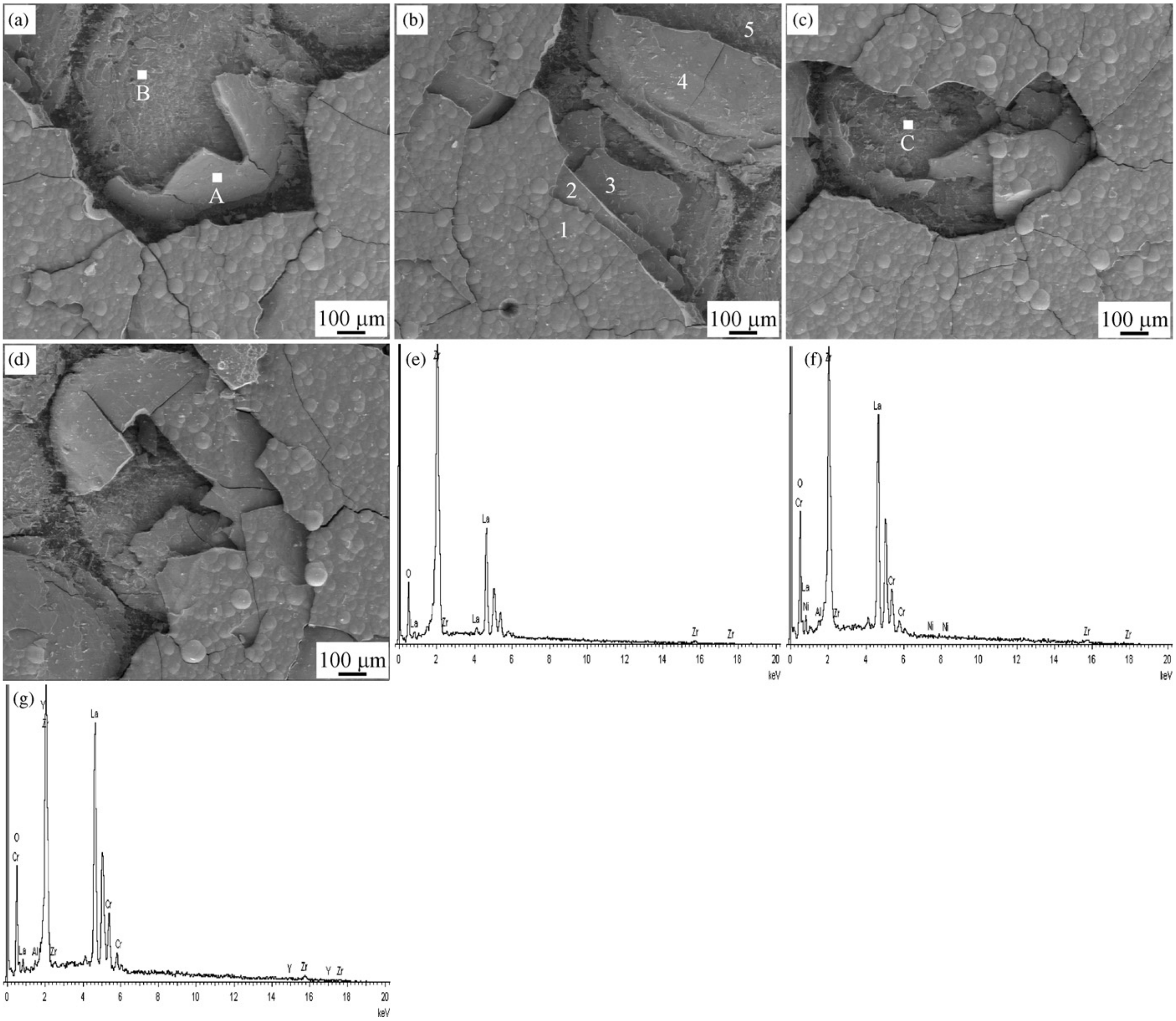

Fig. 6. SEM surface morphologies of the two coatings after spallation: (a) and (b) for LZ, (c) and (d) for LZ3Y. (e)–(g) are EDS spectra of areas "A"–"C", respectively. Numbers 1–5 in (b) indicate that the spalled coating can be divided into five layers.

curves for the whole oxidation behaviors of LZ and LZ3Y coatings are also obtained after fitting the experimental data, which can be described respectively as:

$$\Delta M_{\mathrm{LZ}} = -1.47\times10^{-10}\mathrm{N}^4 + 1.46\times10^{-7}\mathrm{N}^3 - 5.27\times10^{-5}\mathrm{N}^2 + 8.07\times10^{-3}\mathrm{N} + 8.49\times10^{-2} \qquad (7)$$

$$\Delta M_{\mathrm{LZ3Y}} = -1.02\times10^{-10}\mathrm{N}^4 + 1.20\times10^{-7}\mathrm{N}^3 - 4.95\times10^{-5}\mathrm{N}^2 + 8.37\times10^{-3}\mathrm{N} + 5.74\times10^{-2} \qquad (8)$$

where ΔM is weight change, N is thermal cyclic number.

Fig. 6 shows the SEM images of the LZ and LZ3Y coatings' surfaces after failure and the corresponding EDS analyses. Although grain boundaries between columnar grains have almost disappeared for the two coatings after thermal cycling, column tips observed in Fig. 6a–d still present cauliflower-like appearance that is the characteristic microstructure of EB-PVD coating, indicating that both LZ and LZ3Y materials have low sintering ability. As presented in Fig. 6a–d, the microcracks with a width of about 6–8 μm originated on the surfaces of LZ and LZ3Y coatings are observed. The possible reason is that the top ceramic coating is subjected to a tensile stress during heating. Microcracks between columnar grains could be easily induced because microcracks are able to release stresses in the ceramic coating [29]. It is expected that those microcracks would be beneficial in extending the thermal cycling life of TBCs when they do not grow on a large scale [30]. Furthermore, several microcracks are carefully observed inside of LZ coating as shown in Fig. 6a and b and the coating surface is simultaneously divided into five layers (Fig. 6b), implying that the spallation of LZ coating induced by transverse cracks may be the first emergence of delamination followed by spalling layer by layer. However, the spallation of LZ3Y coating is probably similar to the failure mode of YSZ coating [30]. From Fig. 6c and d, the delamination of LZ3Y coating is clearly observed after spallation. Because EDS result presented in Fig. 6e (area "A") shows that only La, Zr and O are detected. To give further evidence of this phenomenon, the EDS analysis of area "B" is carried out. Although the relative contents of La, Zr and O are high, several alloying elements such as Ni, Cr and Al are also detected (Fig. 6f). It demonstrates that the spallation location of LZ coating is likely to occur either in the interface of LZ and bond

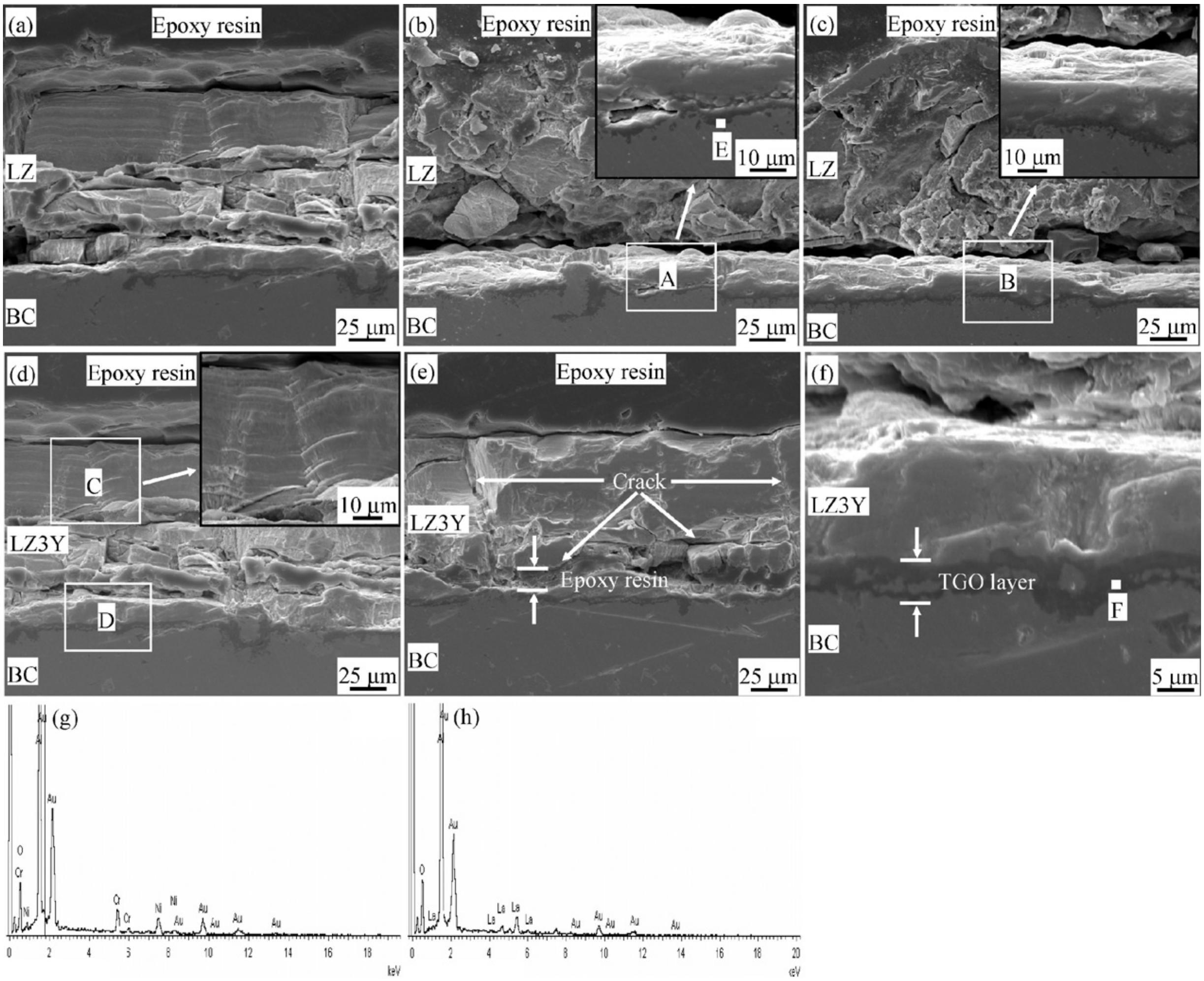

Fig. 7. Cross-sectional SEM images of the two coatings after spallation: (a)–(c) for LZ, (d) and (e) for LZ3Y. (f) is the enlarged image of area “D” in (d). Insets of panels (b)–(d) are the enlarged images of areas “A”–“C”, respectively. (g) and (h) are EDS spectra of areas “E” and “F”, respectively.

coat or inside of LZ coating. The EDS analysis of area “C” (Fig. 6g) shows that the relative contents of La, Zr, Y and O are very high, but content of other element such as Cr is low, indicating that the spallation location of the LZ3Y coating probably occurs within the ceramic coating. This spallation mode seems to be similar to the LZ coating. The appearance of alloying elements within LZ and LZ3Y coatings demonstrates that the alloying elements of Ni, Cr and Al in bond coat perhaps have diffused into the ceramic coatings.

The cross-sectional SEM images of the LZ and LZ3Y coatings after thermal cycling test are presented in Fig. 7. After thermal cycling, a black thin layer with a thickness of about 7 μm between the ceramic coating and BC is clearly observed in Fig. 7a–f, and this thin layer is the thermally grown oxide (TGO) layer, implying that BC oxidation is still an important factor for coating failure. The internal oxidation of BC usually occurs by both the oxygen penetration through the inter-columnar gaps in the ceramic coat and oxygen-diffusion through the crystal lattice of the coating material [31]. The TGO layer observed in Fig. 7a–c is very dense and the phenomenon of internal oxidation of BC is also evident. However, for the LZ3Y coating, the growth of TGO layer is incomplete and it is also hard to measure the exact thickness of TGO layer (Fig. 7d–f). In other words, the BC oxidation in LZ3Y coating is weaker than that in LZ coating. It seems that this phenomenon is consistent with the results shown in Fig. 5. The TGO layer consists of mainly Al_2O_3 and some oxides of Ni and Cr as proved by EDS (Fig. 7e and g). The composition of TGO layer in LZ3Y coating is mostly Al_2O_3, only a small quantity of La_2O_3 coexisted (Fig. 7f and h). The higher is the content of pure Al_2O_3 in the TGO layer, the longer is the thermal cycling life of TBCs [32].

It is generally known that the location of delamination and cracks is mostly within the TGO layer for EB-PVD coatings. It is carefully seen from Fig. 7b that some cracks and pores appear in the interface of LZ and TGO layer. It is considered that the spinel phase of $Ni(Cr, Al)_2O_4$ could be largely accumulated into the outer region of TGO layer, which is very brittle and harmful to reduce the interface bonding. On the other hand, at high temperatures, the $LaAlO_3$ might be formed due to the chemical reaction between excess La_2O_3 and the as-formed Al_2O_3 at the interface between LZ and TGO layer. $LaAlO_3$ has perovskite structure above 723 K and it undergoes a phase transformation to a rhombohedral symmetry as the temperature is decreased, which results in a structure inhomogeneity [33,34]. This could influence the thermal cycling life of TBCs. Additionally, as shown in Fig. 7e, significant crack propagation and delamination at the LZ3Y/TGO interface are also observed, which will have a significant impact on the durability of TBCs, and further lead to TBCs spallation. The additional stress, i.e. growth stress, associated with the TGO growth is one of the main factors for the crack growth and spallation failure of TBCs [35]. According to the EDS result from Fig. 7h, the formation of $LaAlO_3$ in the interface of LZ3Y and TGO layer might be the reason responsible for debonding of ceramic coating from BC surface. In order to study the stabilities of LZ and LZ3Y coatings when they contact TGO, a mixture of LZ and Al_2O_3 (or LZ3Y and Al_2O_3) powders in a molar ratio of 50:50 was heated at 1373 K for 24 h, and the XRD results

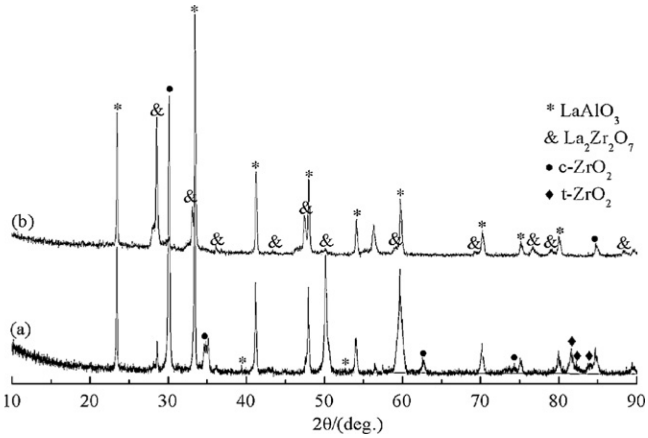

Fig. 8. XRD patterns of the mixtures after being heated at 1373 K for 24 h: LZ coating and Al_2O_3 (a), LZ3Y coating and Al_2O_3 (b).

are shown in Fig. 8. Obviously, the peaks belonging to $LaAlO_3$ are detected in Fig. 8a and b, which further prove that the LZ and LZ3Y coatings could react with the as-formed TGO layer during thermal cycling. The possible reactions are following:

$$La_2Zr_2O_7 + Al_2O_3 = 2LaAlO_3 + 2ZrO_2 \qquad (9)$$

$$La_2O_3 + Al_2O_3 = 2LaAlO_3 \qquad (10)$$

It can be carefully seen from Fig. 8 that the peak intensities of pyrochlore structure (LZ) in LZ3Y coating are accordingly stronger than that of LZ coating under the same experimental conditions. The possible reason is that the coexistence of other phases such as t'-$Y_{0.08}Zr_{0.92}O_{1.96}$ and $YO_{1.401}$ in LZ3Y coating can partially obstruct contact areas of LZ and La_2O_3 particles with Al_2O_3, and further decrease the Gibbs free energies for reactions (9) and (10). Hence it is reasonably assumed that the chemical reaction in Fig. 8b is not so obvious as that in Fig. 8a.

The interfacial thermal stress is the main factor of crack initiation and extension. If the stress state exceeds the adhesive or cohesive bond strength of the coating, delamination and spallation may occur [36]. Fig. 7b and c exhibits a typical cleavage at the interface between LZ and BC, which is probably initiated by the compressive stresses in the cooling process. It is considered that when the compressive stresses are built up so much that become larger than the combination force of LZ/BC interface during thermal cycling, the spallation will occur by disconnection of LZ coating from BC. However, for the LZ3Y coating, this phenomenon is only observed in Fig. 7e. In most cases, the spallation occurs within the ceramic coating approximately 13–16 μm above its TGO layer. This is probably due to existence of excess La_2O_3 within this zone. Consequently, the spallation of LZ3Y coating occurs during cooling. The selective evaporation of La_2O_3 at the beginning of coating formation could further explain the spallation of LZ coating at the interface between LZ and BC.

It can be seen from Fig. 7a to c that transverse cracks occur not only at the interface between LZ and BC but also in the interior of LZ coating. These phenomena are in accord with the result mentioned in Fig. 6a. Because microcracks are able to release stresses introduced into LZ coating, however, the growth of the microcracks

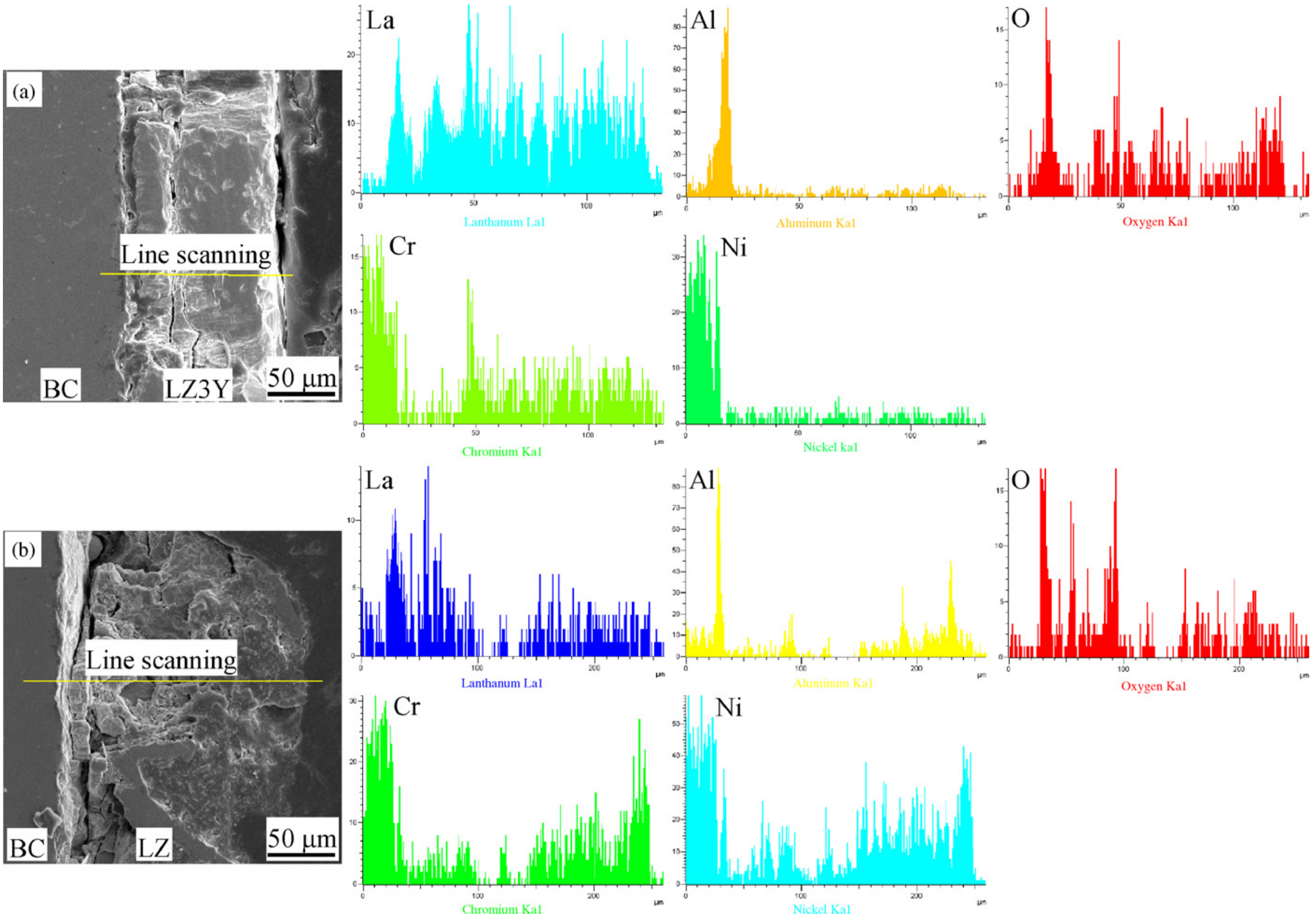

Fig. 9. SEM images and elemental analyses by EDS of LZ3Y (a) and LZ (b) coatings after spallation.

to macrocracks is expected to cause the coating failure. Meanwhile, several transverse cracks and spallation zones inside of LZ coating appeared in Fig. 7a illustrate that the failure of LZ coating may initiate at the surface of LZ coating due to partial sintering of LZ coating surface after long-term cycling, which results in parallel contraction of LZ coating surface. The plane tensile stress is developed in the outer region of LZ coating due to the restriction of the inner region of its coating upon thermal cycling [33]. The transverse cracks in the outer region of LZ coating are developed when the plane tensile stress is accumulated to a certain extent, leading to the spallation of the outer region of LZ coating. This process is repeated and LZ coating spalls gradually layer by layer [33,37]. This result effectively explains why the multi-layer structures are formed within the coating surface as shown in Fig. 6a and b. Although several transverse cracks also appear in Fig. 7d and e, the degree of stress relaxation generated in LZ3Y coating is correspondingly weaker than that of LZ coating. Therefore, the level of degradation and the phenomenon of peeling off the LZ3Y coating in the form of multi-layer are not obvious even cannot be detected. It further confirms that the LZ3Y coating exhibits a good thermal cycling behavior and achieves a prolonged lifetime.

On the other hand, it is also observed in Fig. 7e that the vertical cracks pass through the whole LZ3Y coating and further propagate down to BC surface. As a consequence, the occurrence of transverse cracks within BC surface causes abnormal oxidation of BC and builds up stress growth due to volume swelling, which could reduce the adhesion strength of the interface between LZ3Y coating and BC. In this case, it is considered that air goes through those cracks to reach BC surface and causes the abnormal oxidation of BC [38]. Therefore, a transverse (or vertical) crack develops when the stress, i.e. thermal stress, is accumulated to some extent, leading to the initiative spallation of LZ3Y coating. Similarly, the vertical cracks may also be regarded as a crucial factor for the debonding of LZ coating. It can be seen from Fig. 7d that micro-laminated structure appears apparently in LZ3Y coating, this structure is also observed in LZ coating as presented in Fig. 7a. As previously reported by Guo [39], EB-PVD TBCs with the micro-laminated structure would have a lower thermal conductivity. These phenomena further confirm that rare earth zirconates with pyrochlore structure have a lower thermal conductivity than YSZ. There is no doubt that such micro-laminated structure is beneficial to thermal conductivity reduction of TBCs.

The elemental distributions along the cross-sectional microstructures of LZ3Y and LZ coatings are analyzed by means of EDS and the results are shown in Fig. 9. It is obvious that La element is regularly distributed within LZ3Y coating as compared with LZ coating, it further proves that Y_2O_3 acts as a dopant as well as a process regulator. As expected, contents of Al and O are very high in the interface of these two ceramic coatings and BC, implying that TGO in LZ3Y and LZ coatings consists of mainly Al_2O_3. This phenomenon is consistent with the results of Fig. 7g and h. Surprisingly, the alloying element of Cr in BC has partially diffused into LZ3Y and LZ coatings as shown in Fig. 9. In contrast, the peak intensity of Cr element within LZ coating is correspondingly stronger than that of LZ3Y coating, demonstrating that the diffusion velocity of Cr in the former is faster than in the latter. Similarly, Ni and Al are also detected in LZ coating, but they do not appear in LZ3Y coating. Because the columns of LZ coating are more regularly distributed and the inter-columnar gaps are narrower compared with LZ3Y coating. This microstructure provides the path for outward diffusion of alloying elements into the ceramic coating. As previously reported by Thornton et al. [40], chemical reactions of the ceramic coating with Cr, Al and Ni were possible by outward diffusion of alloying elements into BC. In order to study the stabilities of LZ and LZ3Y coatings when they contact alloying elements, the mixtures of LZ and Cr_2O_3 (or LZ3Y and Cr_2O_3) powders and LZ and Ni_2O_3 (or LZ3Y and Ni_2O_3) powders were heated at 1373 K for 48 h, and the XRD results are shown in Fig. 10. Obviously, the peaks belonging to $LaCrO_3$ are detected in Fig. 10a and b, and the peak intensities of $LaCrO_3$ in LZ3Y coating are stronger than that of LZ coating. This result directly explains why the content of Cr_2O_3 accumulated interior of LZ3Y coating is accordingly higher compared with LZ coating. The relevant relationship can be expressed as:

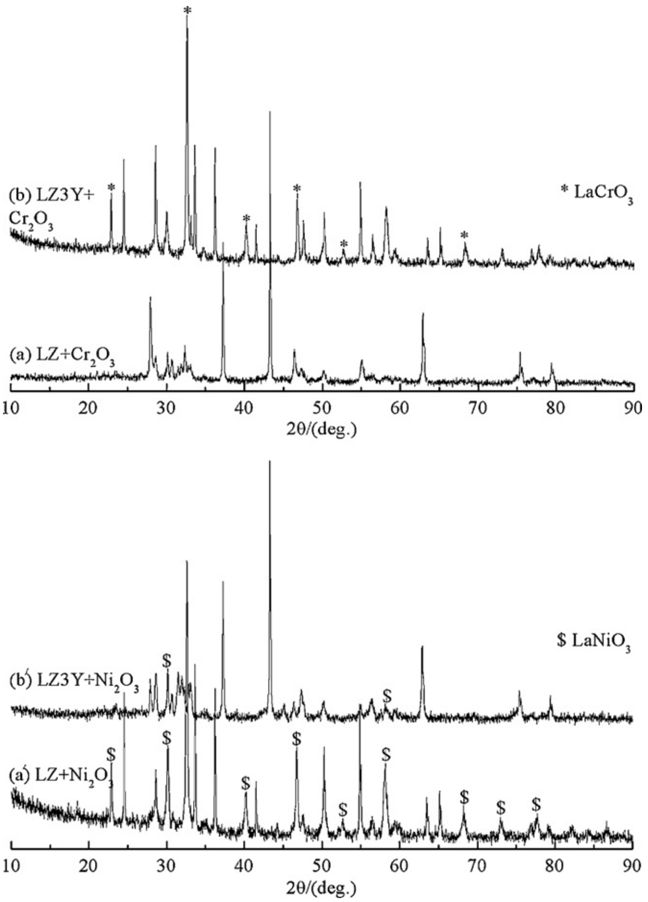

Fig. 10. XRD patterns of the mixtures after being heated at 1373 K for 48 h: LZ coating and Cr_2O_3 (a), LZ3Y coating and Cr_2O_3 (b), LZ coating and Ni_2O_3 (a′), LZ3Y coating and Ni_2O_3 (b′).

$$La_2Zr_2O_7 + Cr_2O_3 = 2LaCrO_3 + 2ZrO_2 \tag{11}$$

$$La_2O_3 + Cr_2O_3 = 2LaCrO_3 \tag{12}$$

The crystal structure of $LaCrO_3$ below 513 K and above 553 K is orthorhombic- and rhombohedral-distorted perovskite structure, respectively. The discrete volume compression is observed at the phase transition from orthorhombic to rhombohedral phase, which might generate internal stresses and initiate microcracks within the ceramic coatings during heating-up and cooling-down [41].

Similarly, peaks of $LaNiO_3$ are clearly detected in Fig. 10a′, but only two weak peaks of $LaNiO_3$ appear in Fig. 10b′. These results are reasonable to suggest that chemical reaction of LZ pyrochlore structure with Ni_2O_3 is basically inert, and the excess La_2O_3 is probably the primary factor responsible for occurrence of $LaNiO_3$ within these two ceramic coatings. $LaNiO_3$ has a single perovskite structure below 1273 K. At temperatures of above 1273 K, the following sequence of decomposition occurs upon increasing temperature:

$LaNiO_3 \rightarrow La_4Ni_3O_{10} \rightarrow La_3Ni_2O_7 \rightarrow La_2NiO_4$ as confirmed previously by Zinkevich [42]. This process could be detrimental to the ceramic coatings, because the temperature adopted for thermal cycling is 1373 K. Therefore, chemical reactions of these two ceramic coatings with alloying elements can weaken the chemical stabilities of LZ and LZ3Y coatings, resulting in appearance of microcracks inside these two ceramic coatings. This outward diffusion may eventually lead to premature failure of LZ and LZ3Y coatings. In the present work, the thermal cycling test was performed at 1373 K that is relatively lower than the target temperature for applications of LZ and LZ3Y coatings. A burner-rig test with higher gas temperature is still in progress in order to evaluate the higher temperature capability and thermal cycling lifetime of LZ and LZ3Y coatings above 1523 K.

4. Conclusions

Ceramic coatings with compositions of LZ and LZ3Y had been fabricated by EB-PVD, and the phase structures, columnar microstructures and thermal cycling behaviors were systematically compared and investigated. The conclusions are following:

(1) The LZ3Y coating has a longer thermal cycling life than that of LZ coating. The improvement of chemical homogeneity of the coating, the superior growth behavior of columns and the favorable mechanical properties are all very helpful to the prolongation of thermal cycling life of LZ3Y coating. A way to further improve the life of LZ3Y coating could be in the use of YSZ coating as the interlayer between the LZ3Y and the bond coat. Alternatively, a thin layer (<5 μm) acts as diffusion barrier between the LZ3Y and the bond coat could be fabricated prior to deposition of LZ3Y coating.

(2) The spallation of the LZ3Y coating may occur within the ceramic coating approximately 13–16 μm above its TGO layer, but the spallation of LZ coating is observed at the interface between ceramic coating and bond coat. The excess La_2O_3, chemical incompatibility of the ceramic coatings with TGO layer, the visible cracks initiation, propagation and extension, the abnormal oxidation of BC, the thermal expansion mismatch between ceramic coatings and BC, and the outward diffusion of alloying elements into the ceramic coatings are the primary factors for the spallation of LZ and LZ3Y coatings.

Acknowledgements

The authors gratefully acknowledge the careful manufacture of bond coats by J.P. Li. Financial supports from projects NSFC-50825204, NSFC-20921002 and Hunan Provincial Key Laboratory of Materials Protection for Electric Power and Transportation (Changsha University of Science & Technology) are also gratefully acknowledged.

References

[1] M. Matsumoto, T. Kato, N. Yamaguchi, D. Yokoe, H. Matsubara, Surf. Coat. Technol. 203 (2009) 2835–2840.
[2] Z.-G. Liu, J.-H. Ouyang, Y. Zhou, J. Alloys Compd. 473 (2009) L17–L19.
[3] Z.-G. Liu, J.-H. Ouyang, B.H. Wang, Y. Zhou, J. Li, J. Alloys Compd. 466 (2008) 39–44.
[4] B. Saruhan, P. Francois, K. Fritscher, U. Schulz, Surf. Coat. Technol. 182 (2004) 175–183.
[5] Z.-G. Liu, J.-H. Ouyang, Y. Zhou, J. Alloys Compd. 472 (2009) 311–316.
[6] X.Q. Cao, R. Vassen, W. Jungen, S. Schwartz, F. Tietz, D. Stöve, J. Am. Ceram. Soc. 84 (9) (2001) 2086–2090.
[7] M.J. Maloney, European Patent 0848077 Al (1998).
[8] Z.-G. Liu, J.-H. Ouyang, Y. Zhou, J. Li, J. Alloys Compd. 468 (2009) 350–355.
[9] R. Vassen, X.Q. Cao, F. Tietz, D. Basu, D. Stöver, J. Am. Ceram. Soc. 83 (8) (2000) 2023–2028.
[10] K. Bobzin, E. Lugscheider, N. Bagcivan, High Temp. Mater. Process. 10 (2006) 103–108.
[11] M.A. Subramanian, G. Aravamudan, G.V. Subba-Rao, Prog. Solid State Chem. 15 (1983) 55–143.
[12] Z.H. Xu, X.H. Zhong, J.F. Zhang, Y.F. Zhang, X.Q. Cao, L.M. He, Surf. Coat. Technol. 202 (2008) 4714–4720.
[13] K. Bobzin, E. Lugscheider, N. Bagcivan, Adv. Eng. Mater. 8 (2006) 653–657.
[14] B. Saruhan, K. Frischer, U. Schulz, Ceram. Eng. Sci. Proc. 24 (2003) 491–496.
[15] Z.H. Xu, L.M. He, X.H. Zhong, J.F. Zhang, X.L. Chen, H.M. Ma, X.Q. Cao, J. Alloy. Compd. 480 (2009) 220–224.
[16] A.G. Evans, E.A. Charles, J. Am. Ceram. Soc. 7–8 (59) (1976) 371–372.
[17] M.O.D. Jarligo, Y.S. Kang, A. Kawasaki, Key Eng. Mater. 317–318 (2006) 31–36.
[18] B.P. Manda, V. Grover, M. Roy, A.K. Tyagi, J. Am. Ceram. Soc. 90 (2007) 2961–2965.
[19] J. Nair, P. Nair, B.M. Docsburg, G.V. Ommen, R.H. Ross, A.J. Burggraaf, F. Mizukami, J. Am. Ceram. Soc. 82 (8) (1999) 2066–2072.
[20] O. Yamaguchi, H. Kawabata, H. Hashimoto, K. Shimizu, J. Am. Ceram. Soc. 70 (6) (1987) C131–C132.
[21] U. Schulz, S.G. Terry, C.G. Levi, Mater. Sci. Eng. A 360 (2003) 319–329.
[22] Q.L. Wei, H.B. Guo, S.K. Gong, H.B. Xu, Thin Solid Films 516 (2008) 5736–5739.
[23] R. Subramanian, S.M. Sabol, J. Goedjen, M. Arana, ATS Review Meeting, November 8–10, 1999.
[24] B.A. Movchan, A.V. Demischin, Phys. Met. Metallogr. 28 (1968) 83–90.
[25] U. Leushake, T. Krell, U. Schulz, M. Peters, W.A. Kaysser, B.H. Rabin, Surf. Coat. Technol. 94–95 (1997) 131–136.
[26] U. Schulz, B. Saruhan, K. Fritscher, C. Leyens, Int. J. Ceram. Technol. 1 (4) (2004) 302–315.
[27] L.M. He, Y.-F. Su, L.F. Allard, M.J. Lance, W.Y. Lee, Metall. Mater. Trans. A 35 (13) (2004) 1113–1124.
[28] S.Q. Guo, D.R. Mumm, A.M. Karlsson, Y. Kagawa, Scr. Mater. 53 (2005) 1043–1048.
[29] R.J.L. Steenbakker, R.G. Wellman, J.R. Nicholls, Surf. Coat. Technol. 201 (2006) 2140–2146.
[30] X.F. Bi, H.B. Xu, S.K. Gong, Surf. Coat. Technol. 130 (2000) 122–127.
[31] R.A. Miller, Surf. Coat. Technol. 30 (1987) 1–11.
[32] L.M. He, Mater. Sci. Forum 546–549 (2007) 1781–1788.
[33] W. Ma, S.K. Gong, H.F. Li, H.B. Xu, Surf. Coat. Technol. 202 (2008) 2704–2708.
[34] X. Wang, U. Helmersson, J. Birch, W. Ni, J. Cryst. Growth 171 (3/4) (1997) 401–408.
[35] R. Vassen, G. Kerkhoff, D. Stöver, Mater. Sci. Eng. A 303 (2001) 100–109.
[36] J.W. Hutchinson, A.G. Evans, Surf. Coat. Technol. 149 (2002) 179–184.
[37] M.S. Ali, S. Song, P. Xiao, J. Mater. Sci. 37 (10) (2002) 2097–2102.
[38] H.B. Xu, S.K. Gong, L. Deng, Thin Solid Films 334 (1998) 98–102.
[39] H.B. Guo, S.K. Gong, K.A. Khor, H.B. Xu, Surf. Coat. Technol. 168 (2003) 23–29.
[40] J. Thornton, A. Majumdar, G. McAdam, Surf. Coat. Technol. 94–95 (1997) 112–117.
[41] T. Hashimoto, N. Tsuzuki, A. Kishi, K. Takagi, K. Tsuda, M. Tanaka, K. Oikawa, T. Kamiyama, K. Yoshida, H. Tagawa, M. Dokiya, Solid State Ionics 132 (2000) 183–190.
[42] M. Zinkevich, N. Solak, H. Nitsche, M. Ahrens, F. Aldinger, J. Alloys Compd. 438 (2007) 92–99.